Chapter 14
Nanostructures

The principles of physics, as far as I can see, do not speak against the possibility of maneuvering things atom by atom.

R.P. Feynman, 1959 [1338]

Abstract One-dimensional nanostructures (quantum wires) and zero-dimensional ones (quantum dots) are discussed with regard to their various fabrication methods and the tunable physical properties in such systems. Main effects covered are the modified density of states, confined energy levels, (envelope) wave-function symmetry and the resulting novel electrical and optical properties.

14.1 Introduction

When the structural size of functional elements enters the size range of the de Broglie matter wavelength, the electronic and optical properties are dominated by quantum-mechanical effects. The most drastic impact can be seen from the density of states (Fig. 14.1). The quantization in a potential is ruled by the Schrödinger equation with appropriate boundary conditions. These are simplest if an infinite potential is assumed. For finite potentials, the wavefunction leaks out into the barrier. Besides making the calculation more complicated (and more realistic), this allows electronic coupling of nanostructures. Via the Coulomb interaction, a coupling is even given if there is no wavefunction overlap. In the following, we will discuss some of the fabrication techniques and properties of quantum wires (QWR) and quantum dots (QD). In particular for the latter, several textbooks can also be consulted [1339, 1340].

14.2 Quantum Wires

14.2.1 V-Groove Quantum Wires

Quantum wires with high optical quality, i.e. high recombination efficiency and well-defined spectra, can be obtained by employing epitaxial growth on corrugated substrates. The technique is shown schematically in Fig. 14.2. A V-groove is etched, using, e.g., an anisotropic wet chemical etch, into a GaAs substrate. The groove direction is along $[1\bar{1}0]$. Even when the etched pattern is not very sharp on the bottom, subsequent growth of AlGaAs sharpens the apex to a self-limited radius ρ_l of the order

M. Grundmann, *The Physics of Semiconductors*, Graduate Texts in Physics,
https://doi.org/10.1007/978-3-030-51569-0_14

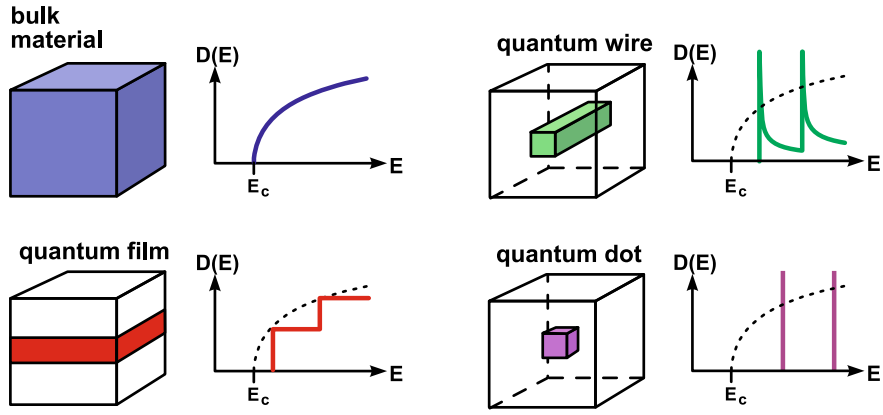

Fig. 14.1 Schematic geometry and density of states for 3D, 2D, 1D and 0D electronic systems

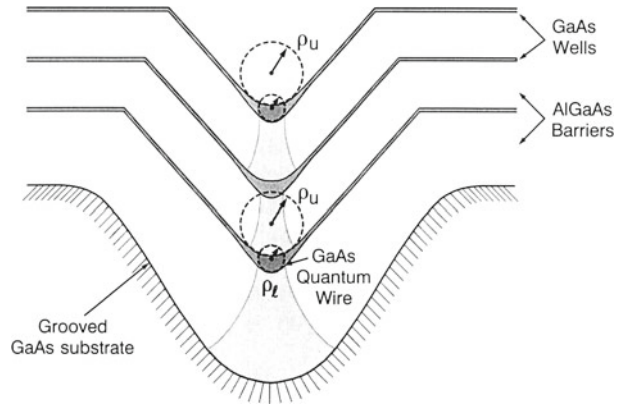

Fig. 14.2 Schematic cross section of a GaAs/AlGaAs heterostructure grown on a channeled substrate, illustrating the concept of self-ordered quantum-wire fabrication. Adapted from [1341], reprinted with permission, ©1992, Elsevier Ltd

of 10 nm. The side facets of the groove are {111}A. Subsequent deposition of GaAs leads to a larger upper radius $\rho_u > \rho_l$ of the heterostructure. The GaAs QWR formed in the bottom of the groove is thus crescent-shaped as shown in Fig. 14.3a. A thin GaAs layer also forms on the side facets (sidewall quantum well) and on the top of the ridges. Subsequent growth of AlGaAs leads to a resharpening of the V-groove to the initial, self-limited value ρ_l. The complete resharpening after a sufficiently thick AlGaAs layer allows vertical stacking of crescent-shaped QWRs of virtually identical size and shape, as shown in Fig. 14.3b. In this sense, the self-limiting reduction of the radius of curvature and its recovery during barrier-layer growth leads to self-ordering of QWR arrays whose structural parameters are determined solely by growth parameters. The lateral pitch of such wires can be down to 240 nm.

To directly visualize the lateral modulation of the band gap, a lateral cathodoluminescence (CL) linescan perpendicular across the wire is displayed in Fig. 14.4. In Fig. 14.4a, the secondary electron (SE) image of the sample from Fig. 14.3a is shown in plan view. The top ridge is visible in the upper and lower parts of the figure, while in the middle the sidewalls with the QWR in the center are apparent. In Fig. 14.4b, the CL spectrum along a linescan perpendicular to the wire (as indicated by the white line in Fig. 14.4a) is displayed. The x-axis is now the emission wavelength, while the y-axis is the lateral position along the linescan. The CL intensity is given on a logarithmic scale to display the full dynamic range. The top QW shows almost no variation in band gap energy ($\lambda = 725$ nm); only directly at the edge close to the sidewall does a second peak at lower energy ($\lambda = 745$ nm) appear, indicating a thicker region there. The sidewall QW exhibits a recombination wavelength of 700 nm at the edge to the top QW, which gradually increases to about 730 nm at the center of the V-groove. This directly

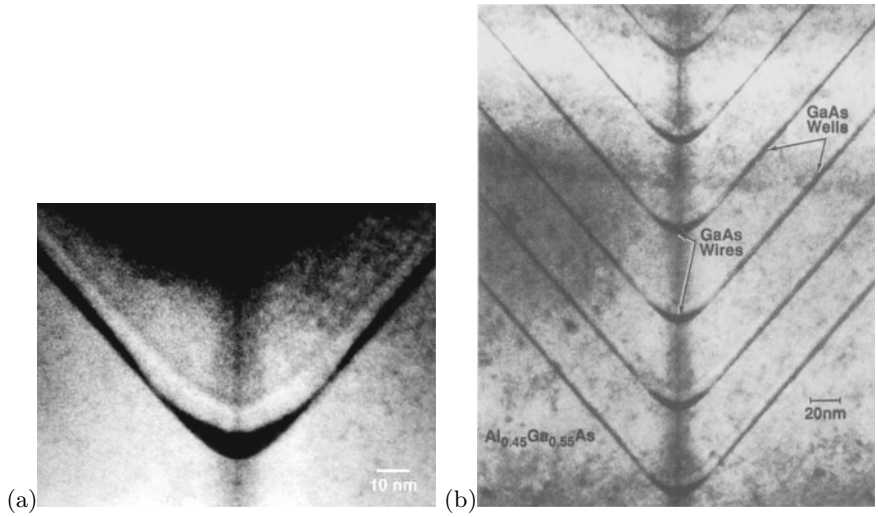

Fig. 14.3 **a** Transmission electron microscopy cross-sectional image of a crescent-shaped single GaAs/AlGaAs quantum wire. From [1342], reprinted with permission, ©1994 IOP. (**b**) TEM cross-sectional image of a vertical stack of identical GaAs/AlGaAs crescent-shaped QWRs. From [1341], reprinted with permission, ©1992, Elsevier Ltd

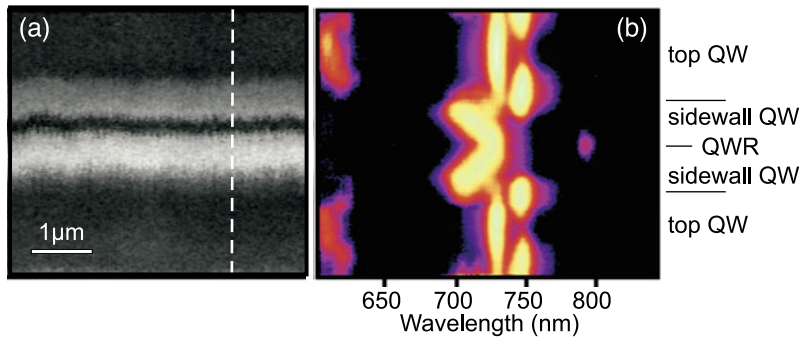

Fig. 14.4 **a** Plan-view SE image of single QWR, showing top and sidewall with QWR in the center. The *white dashed line* indicates the position of the linescan on which the CL spectra linescan **b** has been taken at $T = 5\,\mathrm{K}$. The CL intensity is given on a logarithmic false color scale to display the full dynamic range as a function of wavelength and position. Adapted from [1342], reprinted with permission, ©1994 IOP

visualizes a linear tapering of the sidewall QW from about 2.1 nm thickness at the edge to 3 nm in the center. The QWR luminescence itself appears at about 800 nm.

After fast capture from the barrier into the QWs and, to a much smaller extent corresponding to its smaller volume, into the QWR, excess carriers will diffuse into the QWR via the adjacent sidewall QW and the vertical QW. The tapering of the sidewall QW induces an additional drift current.

14.2.2 Cleaved-Edge Overgrowth Quantum Wires

Another method to create quantum wires of high structural perfection is cleaved-edge overgrowth (CEO) [1343], shown schematically in Fig. 14.5. First, a layered structure is grown (single or multiple quantum wells or superlattice). Then, a {110} facet is fabricated by cleaving (in vacuum) and epitaxy

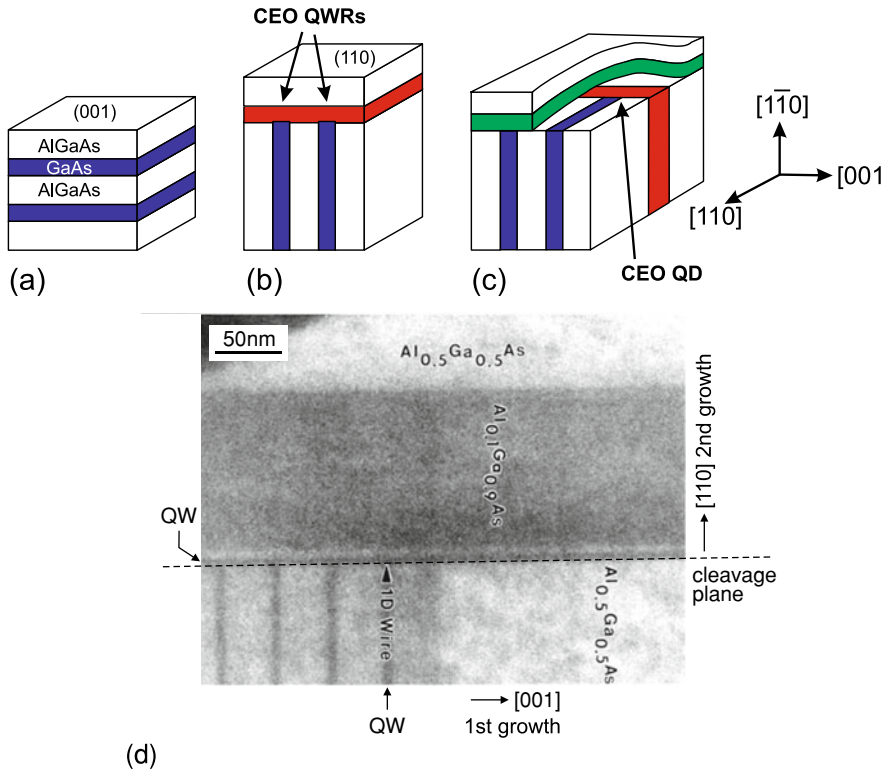

Fig. 14.5 Principle of CEO quantum wires and 2-fold CEO quantum dots. Part (**a**) depicts a layered structure (quantum wells or superlattice, *blue*), (**b**) describes the growth on the cleaved facet used for fabrication of quantum wires. In (**c**) a second cleave and growth on top of the plane allows the fabrication of quantum dots. From [1344]. (**d**) Cross-sectional TEM image of CEO GaAs/AlGaAs quantum wires. Two quantum wells (QW) and the QWR at their junction are labeled. The first epitaxy was from left to right. The second epitaxy step was on top of the cleavage plane (*dashed line*) in the upward direction. Adapted from [1345], reprinted with permission, ©1997 APS

is continued on the cleaved facet. At the junctures of the {110} layer and the original quantum wells QWRs form. Due to their cross-sectional form they are also called *T-shaped* QWRs. A second cleave and another growth step allow fabrication of CEO quantum dots [1344, 1345] (Fig. 14.5c).

14.2.3 Nanowhiskers

Whiskers are primarily known as thin metal spikes and have been investigated in detail [1346]. Semiconductor whiskers can be considered as (fairly short) quantum wires. They have been reported for a number of materials, such as Si, GaAs, InP and ZnO [1347]. A field of ZnO whiskers is shown in Fig. 14.6. If heterostructures are incorporated along the whisker axis [1348], quantum dots or tunneling barriers can be created (Fig. 14.7a). The growth mode relies often a VLS (vapor-liquid-solid) mechanism in which the wire materials are first incorporated into a liquid catalyzer (most often gold) drop at the tip and then used to build up the nanocrystal. In [1349], the layer-by-layer growth of a GaAs nanowire via this mechanism has been observed in-situ by TEM (Fig. 14.7b) and is also available as an impressive video. Another nanowire growth mechanism is the VSS (vapor-solid-solid) mechanism that works without liquid drop on top of the wire.

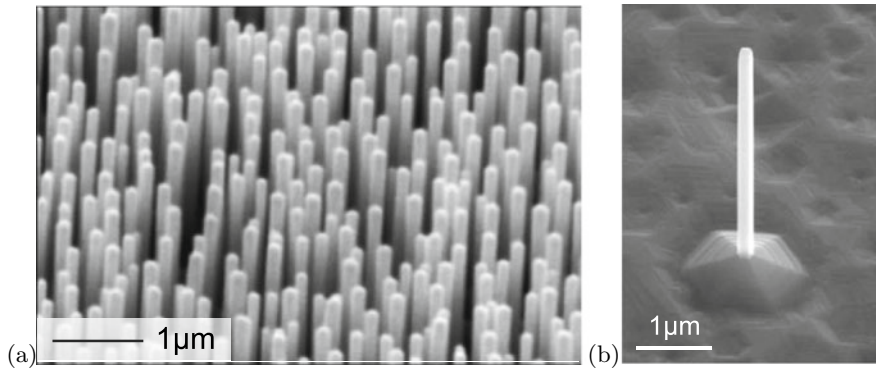

Fig. 14.6 **a** Array of ZnO nanowhiskers on sapphire, fabricated using thermal evaporation. Adapted from [1353]. **b** Single, free-standing ZnO nanowire fabricated using PLD. Adapted from [1354]

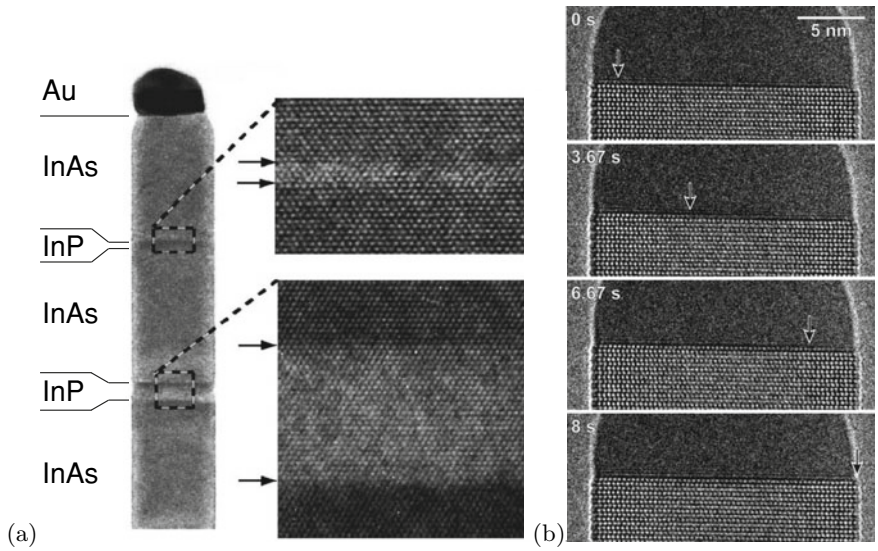

Fig. 14.7 **a** TEM image of a part of an InAs whisker 40 nm in diameter that contains InP barriers. The zooms show sharp interfaces. On top of the whisker is a gold droplet from the so-called vapor–liquid–solid growth mechanism. The whisker axis is [001], the viewing direction is [110]. Adapted from [1348], reprinted with permission, ©2002 AIP. **b** Subsequent growth stages of the tip of a GaAs nanowire with Au cap; times at which (in-situ) TEM image has been taken are labelled. The *arrows* indicate the position of the growth front. Adapted from [1349], reprinted with permission, ©2018 APS

Such nanocrystals can also act as a nanolaser [1350, 1351]. In ZnO nanowhiskers the conversion of mechanical energy into electrical energy has been demonstrated [1352] based on the piezoelectric effect (Sect. 16.4).

The critical thickness h_c in nanowire heterostructure is strongly modified from the 2D situation (Sect. 5.4.1). Based on the strain distribution of a misfitted slab in a cylindrical wire [1355] the dependence of critical thickness on the nanowhisker radius r was developed [1356, 1357]. For given misfit ϵ there is a critical radius r_c for which h_c is infinite for $r < r_c$ (Fig. 14.8).

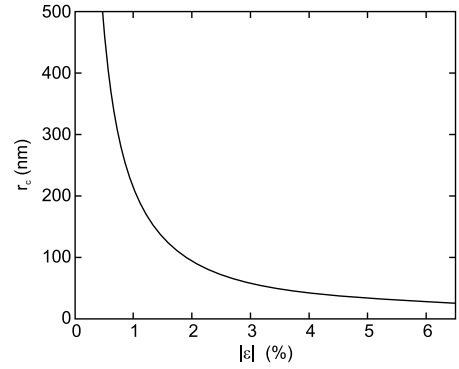

Fig. 14.8 Critical radius r_c above which an infinitely thick layer with misfit ϵ grows coherently on a cylindrical nanowire (relaxation by 60° dislocations, $b = 0.4$ nm, $\nu = 1/3$). Adapted from [1357]

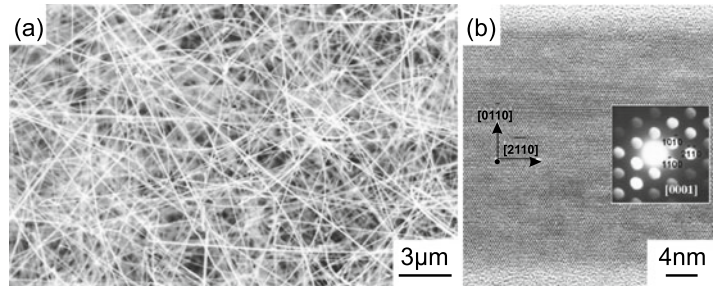

Fig. 14.9 **a** SEM image of an ensemble of ZnO nanobelts. **b** HRTEM image of a single ZnO nanobelt, viewing direction is [00.1]. The *inset* shows the diffraction pattern. Adapted from [1358], reprinted with permission, ©2004 AIP

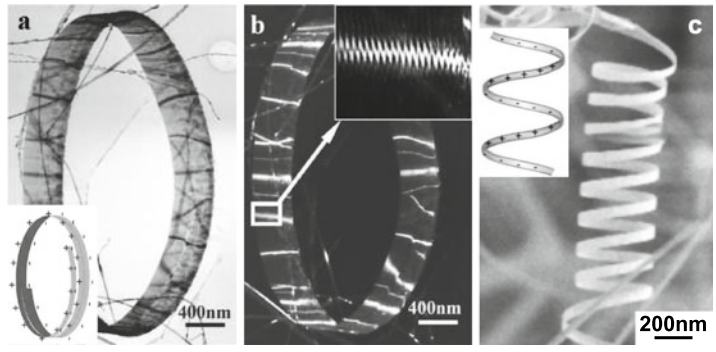

Fig. 14.10 **a** Bright field and **b** dark field TEM image of a ZnO nanoring formed by the 'slinky'-like growth of a nanobelt. **c** SEM image of an open ZnO nanospiral. The *insets* in (**a**, **c**) show schematically the surface charge distribution. Adapted from [1359], ©2006 IOP

14.2.4 Nanobelts

A number of belt-shaped nanostructures has been reported [1347]. These are wire-like, i.e. very long in one dimension. The cross-section is rectangular with a high aspect ratio. In Fig. 14.9a ZnO nanobelts are shown. The wire direction is $[2\bar{1}.0]$. The large surface is (00.1), the thickness of the belt extends in [01.0]-direction. High resolution transmission microscopy (Fig. 14.9b) shows that these structures are defect-free. The pyroelectric charges on the ZnO (0001) surfaces (Sect. 16.2) lead to the formation of open (Fig. 14.10c) spirals. Closed spirals (Fig. 14.10a) occur if the short dimension is along [00.1] and alternating charges become compensated in a 'slinky'-like ring (Fig. 14.10b).

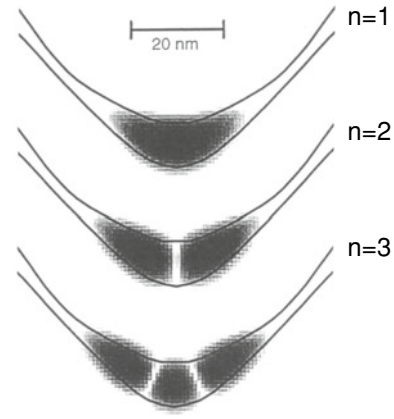

Fig. 14.11 Electron wavefunctions ($|\Psi|^2$ on logarithmic grey scale) for the first three confined levels for the QWR of Fig. 14.3a. From [1342]

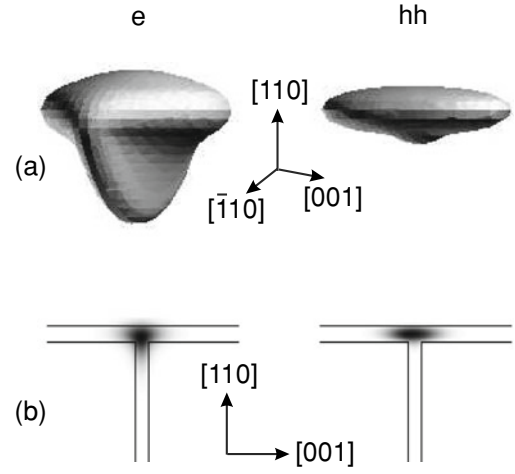

Fig. 14.12 **a** Three-dimensional view of the electron and (heavy) hole part of the excitonic wavefunction in a 4 nm × 5 nm T-shaped $In_{0.2}Ga_{0.8}As/GaAs$ QWR. The orbitals correspond to 70% probability inside. **b** Cross section through the electron and hole orbitals in their center along the wire direction. Reprinted with permission from [1361], ©1998 APS

14.2.5 Quantization in Two-Dimensional Potential Wells

The motion of carriers along the quantum wire is free. In the cross-sectional plane the wavefunction is confined in two dimensions. The simplest case is for constant cross section along the wire. However, generally the cross section along the wire may change and therefore induce a potential variation along the wire. Such potential variation will impact the carrier motion along the longitudinal direction. Also, a twist of the wire along its axis is possible.

In Fig. 14.11, the electron wavefunctions in a V-groove GaAs/AlGaAs QWR are shown. Further properties of V-groove QWRs have been reviewed in [1360]. In Fig. 14.12, the excitonic electron and hole wavefunctions are shown for a (strained) T-shaped QWR.

In Fig. 14.13a the atomic structure of a very thin ZnO nanowhisker with a cross-section consisting of seven hexagonal unit cells is shown. The theoretical one-dimensional band structure [1362] is shown in Fig. 14.13b together with the charge density of the lowest conduction band state (LUMO) and the highest valence band state (HOMO). The band gap is generally too small because of the LDA method used.[1] In [1362] also the properties of nanowires with various diameters are compared. The HOMO at Γ lies only 80 meV above the top of valence band of bulk ZnO, and its position changes little with

[1] The LDA in [1362] yields $E_g = 0.63$ eV for the bulk ZnO band gap; its experimental value is 3.4 eV.

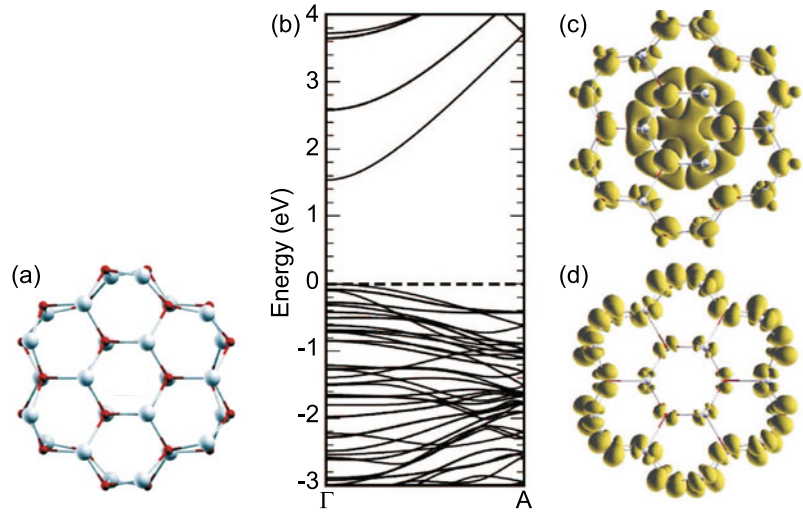

Fig. 14.13 **a** Atomic arrangement of a 1 nm wide ZnO nanowire. **b** Theoretical band structure and charge density of the **c** lowest conduction band and **d** highest valence band state. Adapted from [1362], reprinted with permission, ©2006 AIP

the wire diameter. It is mainly composed by surface oxygen 2p like dangling bonds (Fig. 14.13d). The LUMO (Fig. 14.13c) is delocalized in the whole nanowire, indicating that it is a bulk state. The delocalized distribution is also responsible for the large dispersion of the LUMO from Γ to A. The energy of the LUMO increases substantially with decreasing diameter due to the radial confinement.

14.3 Carbon Nanotubes

14.3.1 Structure

A carbon nanotube (CNT) is a part of a graphene sheet (cf. Sect. 13.1) rolled up to form a cylinder. CNTs were first described as multi-walled nanotubes by Iijima [1363] in 1991 (Fig. 14.14b) and in their single-walled form (Fig. 14.14a) in 1993 [1364]. Reviews can be found in [1247, 1365].

The chirality and diameter of a nanotube are uniquely described by the chiral vector

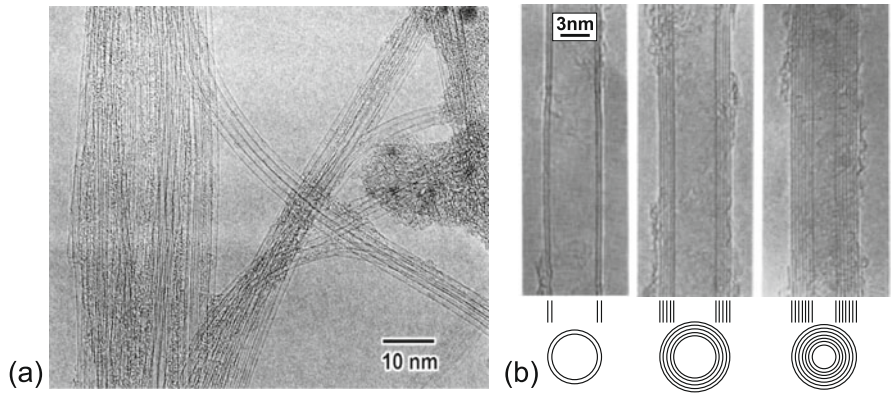

Fig. 14.14 **a** TEM image of single-walled carbon nanotubes (SWNT). **b** TEM images of various multi-walled carbon nanotubes (MWNT). Adapted from [1363], reprinted with permission, ©1991, SpringerNature

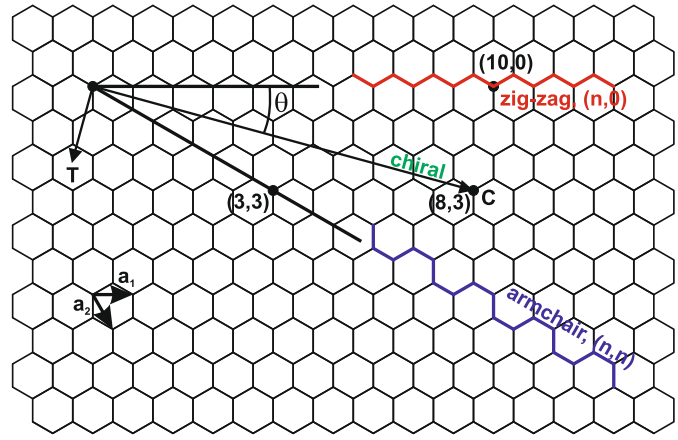

Fig. 14.15 Schematic atomic arrangement in graphene; the C–C bond length is $d_{C-C} = 0.142\,\text{nm}$. Several vectors for making carbon nanotubes (cf. Sect. 14.3) are shown

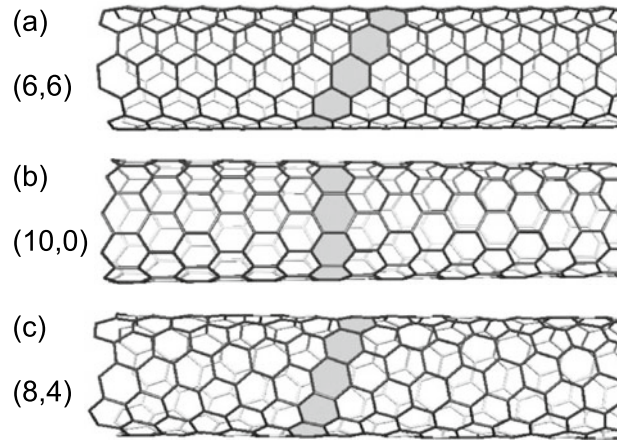

Fig. 14.16 Structure of different types of carbon nanotubes that have similiar diameter of 0.8 nm. **a** Armchair (6, 6), **b** zigzag (8, 0) and **c** chiral symmetry. Adapted from [1247]

$$\mathbf{c}_\text{h} = n_1\,\mathbf{a}_1 + n_2\,\mathbf{a}_2 \equiv (n_1, n_2)\ , \tag{14.1}$$

where $\mathbf{a}_1$ and $\mathbf{a}_2$ are the unit vectors of the graphene sheet. The chiral vector denotes two crystallographic equivalent sites which are brought together along the circumference of the nanotube. The possible vectors are visualized in Fig. 14.15 for $-30° \le \theta \le 0°$. The fiber diameter is given by

$$d = \frac{|\mathbf{c}_\text{h}|}{\pi} = \frac{a}{\pi}\left(n_1^2 + n_1\,n_2 + n_2^2\right)\ , \tag{14.2}$$

with the graphene lattice constant $a = \sqrt{3}\,d_{C-C} = 0.246\,\text{nm}$. Ab-initio calculations show that the diameter becomes a function of the chiral angle below 0.8 nm; deviations from (14.2) are below 2% for tube diameters $d > 0.5\,\text{nm}$ [1366]. The $(n, 0)$ tubes ($\theta = 0$) are termed 'zig-zag' and an example is depicted in Fig. 14.16b. Nanotubes with $\theta = \pm\pi/6$, i.e. of the (n, n) (and $(2n, -n)$) type, are called 'armchair'. All others are termed 'chiral'.

The extension along the wire axis is large compared to the diameter. The tip of a nanotube is part of a buckminster-fullerene type molecule (Fig. 14.17). When the nanotube if formed by rolling a single sheet of graphene (SLG), a single-walled nanotube (SWNT) is formed. A FLG sheet creates a multi-walled nanotube (MWNT). For small number of layers they are called double-walled, triple-walled and so forth.

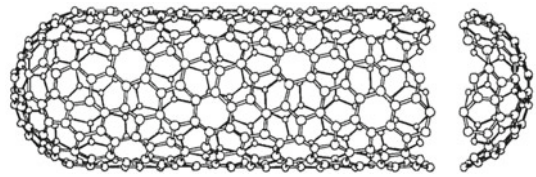

Fig. 14.17 A chiral nanotube (chiral vector is (10, 5), $\theta = -19.11°$) with hemispherical caps at both ends based on an icosahedral C_{140} fullerene. The tube diameter is 1.036 nm. Adapted from [1367]

The mechanical strength of carbon nanotubes is very large. For SWNT Young's moduli of 10^3 GPa have been found experimentally [1368] in agreement with theoretical predictions [1369].

14.3.2 Band Structure

In carbon nanotubes there is some mixing of the $\pi(2p_z)$ and $\sigma(2s \text{ and } 2p_z)$ carbon orbitals due to the radial curvature. This mixing is, however, small and can be neglected near the Fermi level [1370]. The band structure of a nanotube is mainly determined by zone-folding of the graphene band structure. The vector along the (infinitely extended) wire k_z is continuous. The vector $k_\perp$ around the nanotube is discrete with the periodic boundary condition

$$\mathbf{c}_\mathrm{h} \cdot \mathbf{g}_\perp = 2\pi\, m \ , \tag{14.3}$$

where m is an integer. The distance of allowed $k_\perp$-values is (5.5)

$$\Delta k_\perp = \frac{2\pi}{\pi\, d} = \frac{2}{d} \ . \tag{14.4}$$

The character of the nanotube band structure depends on how the allowed k-values lie relative to the graphene Brillouin zone and its band structure. This is visualized in Fig. 14.18. For the case of an armchair tube (n, n), as shown in Fig. 14.18a, the K-point of the graphene band structure always lies on an allowed k-point. Therefore, the nanotube is metallic, i.e. zero-gap, as seen in the bandstructure in Fig. 14.18b. The Dirac point is between Γ and X. For a zig-zag nanotube, the k-space is shown in Fig. 14.18c for a (6, 0) nanotube. The corresponding band structure for a (6, 0) nanotube is also metallic (Fig. 14.18d) with the Dirac point at the Γ point.

In Fig. 14.19c the band structure of another metallic (12, 0) zig-zag nanotube is shown. However, only for (3 m, 0) the K-point is on an allowed state and thus the tube metallic. For the other cases, as shown for the k-space of a (8, 0) nanotube in Fig. 14.19b, this is not the case. The corresponding band structure (Fig. 14.19c for (13, 0)) has a gap and thus the nanotube is a semiconductor. Generally, the condition for a nanotube to be metallic is with an integer m

$$n_1 - n_2 = 3\, m \ . \tag{14.5}$$

There are two semiconducting 'branches' with $\nu = (n_1 - n_2) \bmod 3 = \pm 1$. The tubes with $\nu = +1$ have a small band gap, those with $\nu = -1$ have a larger band gap.

The density of states is a series of one-dimensional DOS, proportional to $\sqrt{E}$ (6.79). It is compared in Fig. 14.20 for a metallic and a semiconducting nanotube. Within 1 eV from the Fermi energy the DOS can be expressed in an universal term [1373].

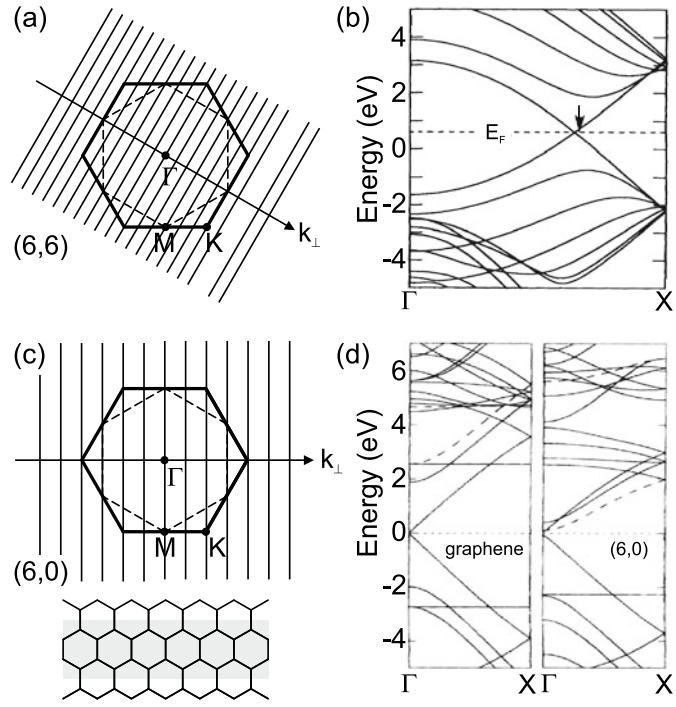

Fig. 14.18 **a** Brillouin zone of the graphene lattice (*bold* line) and allowed k-values for a (6, 6) armchair nanotube. **b** Band structure of a (6, 6) carbon nanotube. Adapted from [1371]. **c** Brillouin zone of the graphene lattice (*bold* line) and allowed k-values for a (6, 0) zig-zag carbon nanotube. In the *lower part* the real space structure is visualized. (**d**) Band structure of graphene (*left*) and a (6, 6) nanotube (*right*). Adapted from [1372]

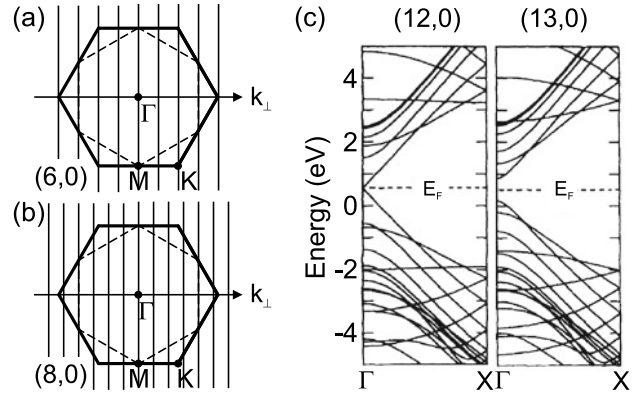

Fig. 14.19 **a**, **b** Brillouin zone of the graphene lattice (*bold* line) and allowed k-values for a (**a**) (6, 0) and a (**b**) (8, 0) zig-zag nanotube. **c** Band structures of a (12,0) metallic and (13, 0) semiconducting armchair carbon nanotube. Adapted from [1371]

14.3.3 Optical Properties

Optical transitions occur with high probability between the van-Hove singularities of the DOS. The theoretical absorption spectrum of a (10, 0) nanotube is shown in Fig. 14.21.

In an ensemble of nanotubes various types and sizes occur. The transition energies of all possible nanotubes sorted by diameter are assembled in the Kataura plot (Fig. 14.22a). Experimental data are shwon in Fig. 14.22b. The two branches of semiconducting nanotubes $\nu = \pm 1$ yield different transition energies. The overall dependence of the transition energy follows a $1/d$-law.

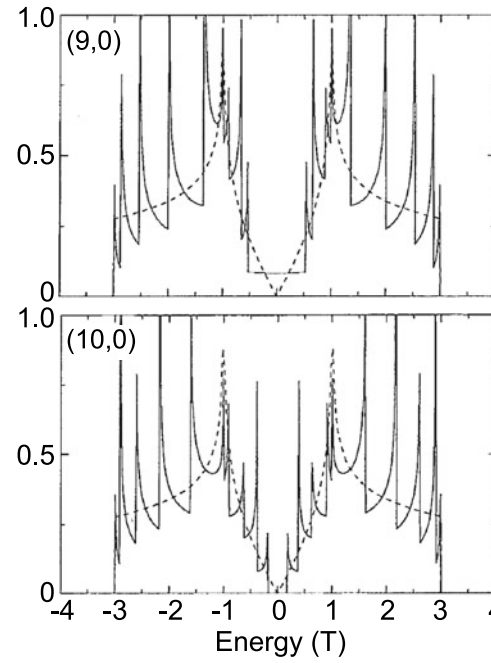

Fig. 14.20 Density of states for a (9, 0) metallic and (10, 0) semiconducting zig-zag carbon nanotube within the tight-binding approximation (13.2). The energy scale is given in units of the tight-binding parameter $T \approx 3\,\text{eV}$. The *dashed lines* are the DOS of graphene. Adapted from [1367]

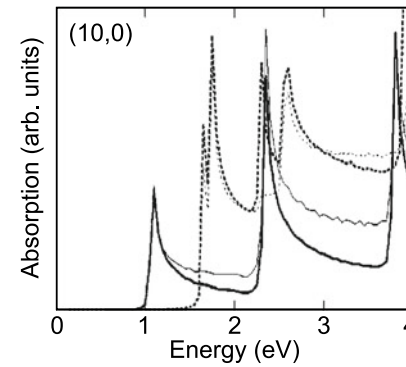

Fig. 14.21 Calculated absorption spectra for a (semiconducting) (10, 0) carbon nanotube for parallel (*solid line*) and perpendicular (*dotted line*) polarization. The *thick* (*thin*) lines are calculated with (without) the matrix element included. Adapted from [1374]

14.3.4 Other Anorganic Nanotubes

Structures similar to carbon nanotubes have been reported for BN [1378, 1379]. A boron nitride nanotube is a cylindrically rolled part of a BN sheet. BN tubes are always semiconducting (Fig. 14.23) and have a band gap beyond 5 eV similar to hexagonal BN which is mostly independent on chirality and diameter [1380]. Thus, while carbon nanotubes appear black since they absorb within 0–4 eV, BN is transparent (or white if scattering). For high energies larger than 10 eV C and BN tubes are quite similar since they are isoelectronic and the high-lying unoccupied states are less sensitive to the difference in the nuclear charges than the states at and below the Fermi energy [1381].

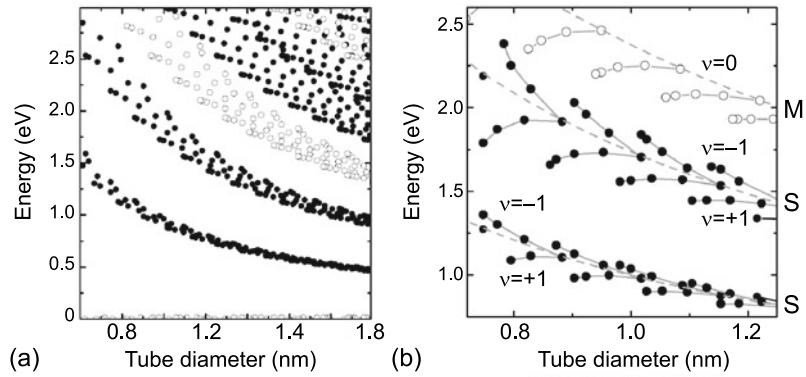

Fig. 14.22 **a** Theoretical transition energies of semiconducting (*filled symbols*) and metallic (*open symbols*) carbon nanotubes as a function of tube diameter (Kataura plot). Energies are calculated from van-Hove singularities in the JDOS within the third-order tight-binding approximation [1252]. **b** Experimental Kataura plot for the first two semiconducting (S, *closed symbols*) and the first metallic (M, *open symbols*) transition. *Dashed lines* connect the (near-to) armchair tubes; *full lines* connect tubes in a branch, $\nu = (n_1 - n_2) \bmod 3$. Data from photoluminescence [1375] and resonant Raman scattering [1376]. Adapted from [1377]

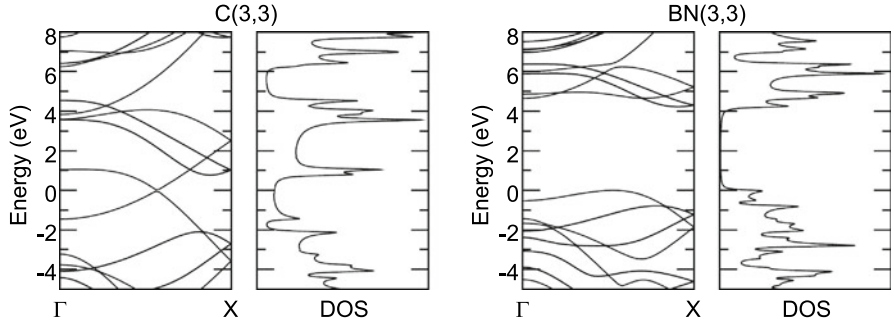

Fig. 14.23 Band structure and density of states (DOS) of C(3,3) and BN(3,3) nanotubes, calculated with DFT-LDA. Adapted from [1381]

14.4 Quantum Dots

14.4.1 Quantization in Three-Dimensional Potential Wells

The solutions for the d-dimensional ($d = 1$, 2, or 3) harmonic oscillator, i.e. the eigenenergies for the Hamiltonian

$$\hat{H} = \frac{\mathbf{p}^2}{2m} + \sum_{i=1}^{d} \frac{1}{2}\, m\, \omega_0^2\, x_i^2 \tag{14.6}$$

are given by

$$E_n = \left(n + \frac{d}{2}\right) \hbar\omega_0 \ , \tag{14.7}$$

with $n = 0, 1, 2, \ldots$. More detailed treatments can be found in quantum-mechanics textbooks.

Next, we discuss the problem of a particle in a centrosymmetric finite potential well with different masses m_1 in the dot and m_2 in the barrier. The Hamiltonian and the potential are given by

$$\hat{H} = \nabla \frac{\hbar^2}{2m} \nabla + V(r) \tag{14.8}$$

$$V(r) = \begin{cases} -V_0 \ , r \leq R_0 \\ 0 \quad , r > R_0 \end{cases} . \tag{14.9}$$

The wavefunction can be separated into radial and angular components $\Psi(\mathbf{r}) = R_{nlm}(r)\ Y_{lm}(\theta, \phi)$, where Y_{lm} are the spherical harmonic functions. For the ground state ($n = 1$) the angular momentum l is zero and the solution for the wavefunction (being regular at $r = 0$) is given by

$$R(r) = \begin{cases} \frac{\sin(k\,r)}{k\,r} & , r \leq R_0 \\ \frac{\sin(k\,R_0)}{k\,R_0}\ \exp\left(-\kappa\ (r - R_0)\right) & , r > R_0 \end{cases} \tag{14.10a}$$

$$k^2 = \frac{2\,m_1\,(V_0 + E)}{\hbar^2} \tag{14.10b}$$

$$\kappa^2 = -\frac{2\,m_2\,E}{\hbar^2} \ . \tag{14.10c}$$

From the boundary conditions that both $R(r)$ and $\frac{1}{m}\frac{\partial R(r)}{\partial r}$ are continuous across the interface at $r = R_0$, the transcendental equation

$$k\,R_0\ \cot\left(k\,R_0\right) = 1 - \frac{m_1}{m_2}\,(1 + \kappa\,R_0) \tag{14.11}$$

is obtained. From this formula the energy of the single particle ground state in a spherical quantum dot can be determined. For a given radius, the potential needs a certain strength $V_{0,\min}$ to confine at least one bound state; this condition can be written as

$$V_{0,\min} = \frac{\pi^2\,\hbar^2}{8\,m^*\,R_0^2} \tag{14.12}$$

for $m_1 = m_2 = m^*$. For a general angular momentum l, the wavefunctions are given by spherical Bessel functions j_l in the dot and spherical Hankel functions h_l in the barrier. Also, the transcendental equation for the energy of the first excited level can be given:

$$k\,R_0\ \cot\left(k\,R_0\right) = 1 + \frac{k^2\,R_0^2}{\frac{m_1}{m_2}\,\frac{2+2\kappa\,R_0+\kappa^2\,R_0^2}{1+\kappa\,R_0} - 2} \ . \tag{14.13}$$

In the case of infinite barriers ($V_0 \to \infty$), the wavefunction vanishes outside the dot and is given by (normalized)

$$R_{nml}(r) = \sqrt{\frac{2}{R_0^3}}\ \frac{j_l(k_{nl}\,r)}{j_{l+1}(k_{nl}\,R_0)} \ , \tag{14.14}$$

where k_{nl} is the n-th zero of the Bessel function j_l, e.g. $k_{n0} = n\pi$. With two-digit precision the lowest levels are determined by

k_{nl}	$l = 0$	$l = 1$	$l = 2$	$l = 3$	$l = 4$	$l = 5$
$n = 0$	3.14	4.49	5.76	6.99	8.18	9.36
$n = 1$	6.28	7.73	9.10	10.42		
$n = 2$	9.42					

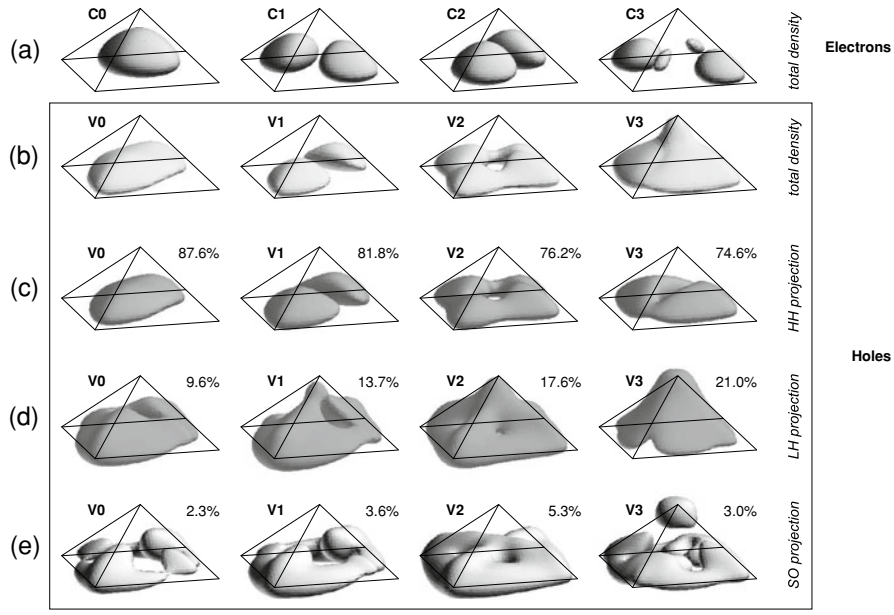

Fig. 14.24 Isosurface plots (25% of maximum value) of the total probability densities **a**, **b** and valence-band projections (**c**)–(**e**) of bound electron (**a**) and hole (**b**)–(**e**) states in a model pyramidal InAs/GaAs quantum dot with base length $b = 11.3\,\text{nm}$. The percentages are the integrals of the projections to the bulk heavy, light and split-off hole bands, respectively, and the isosurfaces show the corresponding projection shapes. For each valence-band state the difference from 100% is the integral $\int_{-\infty}^{\infty} |\psi_{s\uparrow}|^2 + |\psi_{s\downarrow}|^2 \mathrm{d}^3\mathbf{r}$ of the s-type (conduction band) Bloch function projection (not shown). Reprinted with permission from [1385], ©2002, Springer

The $(2l+1)$ degenerate energy levels E_{nl} are ($V_0 = \infty$, $m = m_1$):

$$E_{nl} = \frac{\hbar^2}{2m} k_{nl}^2 \frac{1}{R_0^2} \,. \tag{14.15}$$

The 1s, 1p, and 1d states have smaller eigenenergies than the 2s state.

A particularly simple solution is given for a cubic quantum dot of side length a_0 and infinite potential barriers. One finds the levels $E_{n_x n_y n_z}$:

$$E_{n_x n_y n_z} = \frac{\hbar^2}{2m} \left(n_x^2 + n_y^2 + n_z^2\right) \frac{\pi^2}{a_0^2} \,, \tag{14.16}$$

with $n_x, n_y, n_z = 1, 2, \ldots$. For a sphere, the separation between the ground and first excited state is $E_1 - E_0 \approx E_0$, for a cube and a two-dimensional harmonic oscillator it is exactly E_0. For a three-dimensional harmonic oscillator this quantity is $E_1 - E_0 = 2E_0/3$.

For realistic quantum dots a full three-dimensional simulation of strain, piezoelectric fields and the quantum-mechanical confinement must be performed [1382, 1383]. In Fig. 14.24, the lowest four electron and hole wavefunctions in a pyramidal InAs/GaAs quantum dot (for the strain distribution see Fig. 5.34 and for the piezoelectric fields see Fig. 16.16) are shown. The figure shows that the lowest hole states have dominantly heavy-hole character and contain admixtures of the other hole bands. The wavefunction in such quantum dots can be imaged using scanning tunneling microscopy [1384].

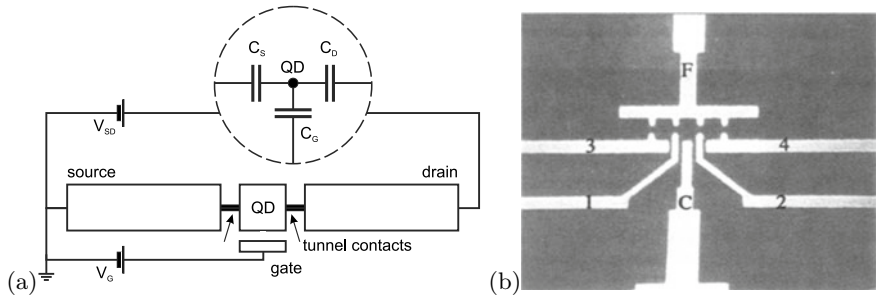

Fig. 14.25 **a** Schematic drawing of a quantum dot (QD) with tunnel contacts and gate electrode. The *inset* depicts an equivalent circuit with capacitances. **b** Realization with an in-plane gate structure. The distance between 'F' and 'C' (gate electrode) is 1 μm. Electron transport occurs from a 2DEG between 3/F to 4/F through the quantum points contacts 1/3 and 2/4. Part (**b**) from [1386], reprinted with permission, ©1991, Springer Nature

14.4.2 Electrical and Transport Properties

The classical electrostatic energy of a quantum dot with capacitance C_G that is capacitively coupled to a gate (Fig. 14.25) at a bias voltage V_G is given by

$$E = \frac{Q^2}{2C_G} - Q\,\alpha\,V_G\,, \tag{14.17}$$

where α is a dimensionless factor relating the gate voltage to the potential of the island and Q is the charge of the island.

Mathematically, minimum energy is reached for a charge $Q_{min} = \alpha\,C_G\,V_G$. However, the charge has to be an integer multiple of e, i.e. $Q = N\,e$. If V_g has a value, such that $Q_{min}/e = N_{min}$ is an integer, the charge cannot fluctuate as long as the temperature is low enough, i.e.

$$kT \ll \frac{e^2}{2\,C_G}\,. \tag{14.18}$$

Tunneling into or out of the dot is suppressed by the Coulomb barrier $e^2/2C_G$, and the conductance is very low. Analogously, the differential capacitance is small. This effect is called *Coulomb blockade*. Peaks in the tunneling current (Fig. 14.26b), conductivity (Fig. 14.26a) and the capacitance occur, when the gate voltage is such that the energies for N and $N+1$ electrons are degenerate, i.e. $N_{min} = N + \frac{1}{2}$. The expected level spacing is

$$e\,\alpha\,\Delta V_G = \frac{e^2}{C_G} + \Delta\epsilon_N\,, \tag{14.19}$$

where $\Delta\epsilon_N$ denotes the change in lateral (kinetic) quantization energy for the added electron. e^2/C will be called the charging energy in the following.

A variation of the source–drain voltage (for a given gate voltage) leads to a so-called Coulomb staircase since more and more channels of conductivity contribute to the current through the device (Fig. 14.27). In Fig. 14.28 the tunneling current is shown as a function of the potential of a dot, formed by gates on a WSe_2 flake [1388], and the source-drain voltage. The iso-current lines form so-called 'Coulomb blockade diamonds'.

The charge Q on the QD is determined by the charges on the gate, source and drain capacities, $Q = Q_G - Q_S + Q_D$. Together with $Q_S = C_S\,V_S$, $Q_D = C_D\,V_D$ and $V_{SD} = V_S + V_D$ and $Q_G =$

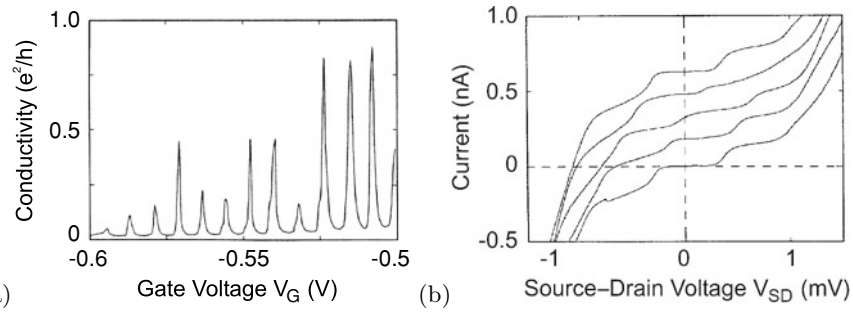

Fig. 14.26 **a** Conductivity (Coulomb oscillations) and **b** current–voltage diagram at different gate voltages (Coulomb staircase, shifted vertically for better readability) of a tunnel junction with a quantum dot as in Fig. 14.25. Adapted from [1386], reprinted with permission, ©1991, SpringerNature

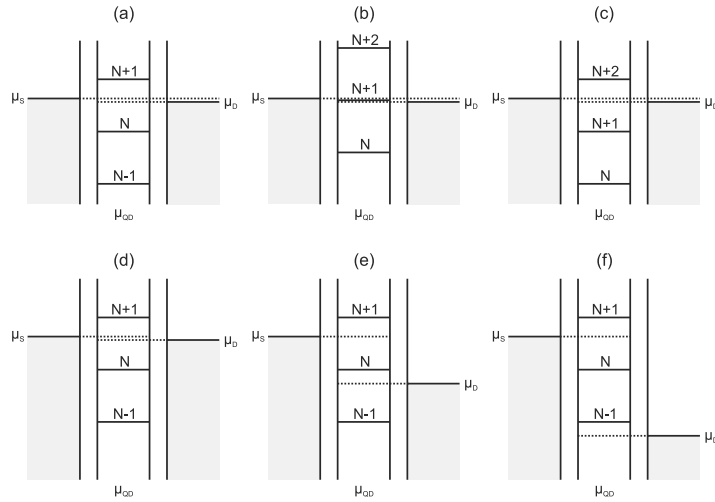

Fig. 14.27 Chemical potentials of source and drain and of a quantum dot in between them. **a**, **b**, and **c** show the sequence for a variation of the gate voltage and visualize the origin of the Coulomb oscillations (see Fig. 14.26a). **d**, **e** and **f** visualize a variation of the source–drain voltage and the origin of the Coulomb staircase (cf. Fig. 14.26b)

$C_G\,(V_G - V_S)$, we find ($C_\Sigma = C_G + C_S + C_D$),

$$V_S = \frac{1}{C_\Sigma}\,(Q + C_G\,V_G + C_D\,V_{SD}) \tag{14.20}$$

$$V_D = \frac{1}{C_\Sigma}\,(-Q - C_G\,V_G + (C_\Sigma - C_D)\,V_{SD})\ . \tag{14.21}$$

Now, if for a given pair of (V_G, V_{SD}) in a diagram like Fig. 14.28b the current is Coulomb-blocked and low, then it is for all voltages with the same charge Q on the dot and either the same V_S or V_D. The derivatives of (14.20) and (14.21) yield the slopes $\partial V_{SD}/\partial V_G = \gamma_1 = -C_G/C_D$ and $\gamma_2 = +C_G/(C_G + C_S)$, respectively, that defined the borders of the diamond in the schematic stability diagram as depicted in Fig. 14.29. We note that such analysis is allowed when $|V_S|, |V_D| \ll e/2C_\Sigma$ and the quantum dot circuit can be treated as a system of capacitors (inset in Fig. 14.25a). Changing Q to $Q - e$ requires V_G to increase by e/C_G for the same $V_{S,D}$, yielding the periodicity of the stability diagram.

Single electron tunneling (SET) circuits [1387] are investigated with respect to metrology for a novel ampere standard [1389].

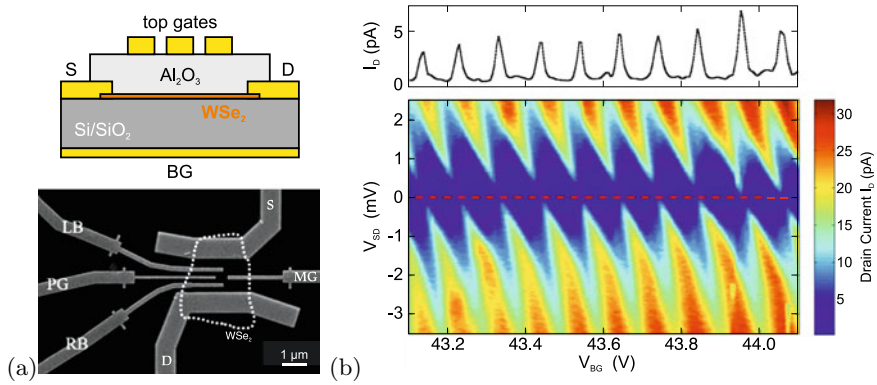

Fig. 14.28 **a** *Top*: Sketch of WSe_2 flake with gate structure, defining a lateral quantum dot. *Bottom*: SEM image of the structure. The outline of the WSe_2 flake (thickness 4.5 nm) is indicated as *dotted line*. BG: back gate, PG: plunger gate. **b** Current (in false colors) as a function of the back gate voltage V_{BG} and the source-drain voltage V_{SD} ($T = 240$ mK). On the top is a current trace as a function of V_G (for $V_{SD} = 0$, along the *red dashed line* in the diagram). SEM image in panel (**a**) and panel (**b**) adapted from [1388] with permission from RSC

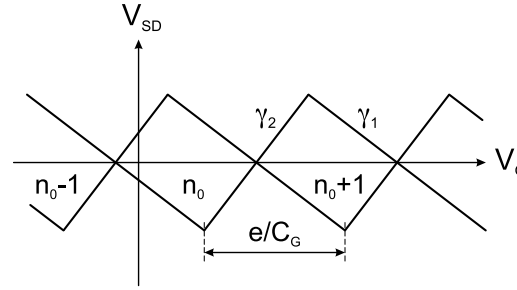

Fig. 14.29 Schematic Coulomb diamond stability diagram. The slopes γ_1 and γ_2 are discussed in the text. The periodicity in the gate voltage is given by e/C_G. The charge on the dot is $Q = (-e)\,n$

A lot of research so far has been done on lithographically defined systems where the lateral quantization energies are small and smaller than the Coulomb charging energy. In this case, periodic oscillations are observed, especially for large N. A deviation from periodic oscillations for small N and a characteristic shell structure (at $N = 2, 6, 12$) consistent with a harmonic oscillator model ($\hbar\omega_0 \approx 3$ meV) has been reported for ≈500-nm diameter mesas (Fig. 14.30b,c). In this structure, a small mesa has been etched and contacted (top contact, substrate back contact and side gate). The quantum dot consists of a 12-nm $In_{0.05}Ga_{0.95}As$ quantum well that is laterally constricted by the 500-nm mesa and vertically confined due to 9- and 7.5-nm thick $Al_{0.22}Ga_{0.68}As$ barriers (Fig. 14.30a). By tuning the gate voltage, the number of electrons can be varied within 0 and 40. Measurements are typically carried out at a sample temperature of 50 mK.

In the sample shown in Fig. 14.31, self-assembled QDs are positioned in the channel under a split-gate structure. In a suitable structure, tunneling through a single QD is resolved.

In small self-assembled quantum dots single-particle level separations can be larger than or similar to the Coulomb charging energy. Classically, the capacitance for a metal sphere of radius R_0 is given as

$$C_0 = 4\pi\,\epsilon_0\,\epsilon_r\,R_0\ , \tag{14.22}$$

e.g.. $C_0 \approx 6$ aF for $R_0 = 4$ nm in GaAs, resulting in a charging energy of 26 meV. Quantum mechanically, the charging energy is given in first-order perturbation theory by

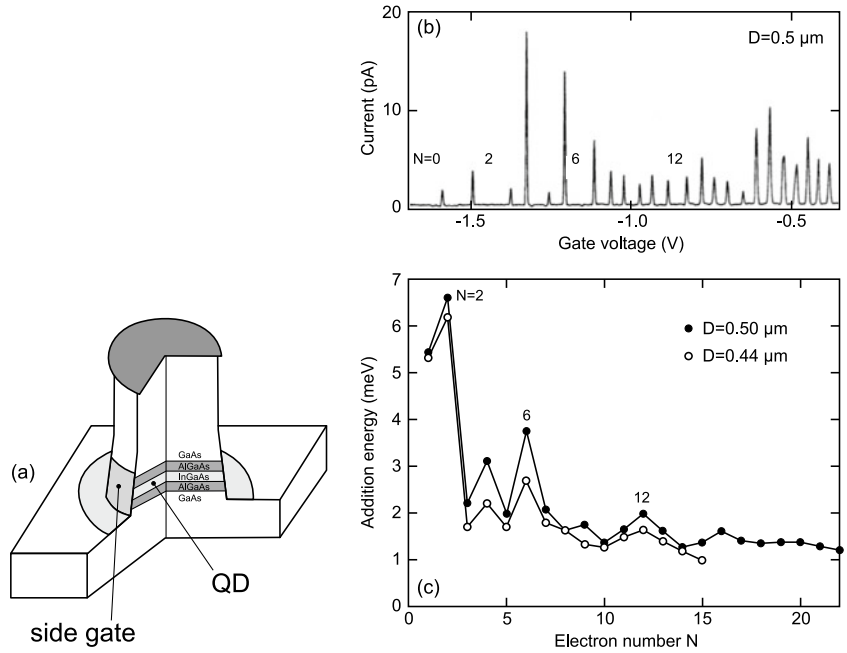

Fig. 14.30 **a** Schematic sample geometry for side-gated $In_{0.05}Ga_{0.95}As/Al_{0.22}Ga_{0.68}As$ disk-shaped quantum dot. **b** Coulomb oscillations in the current versus gate voltage at $B = 0\,\mathrm{T}$ observed for a $D = 0.5\,\mu\mathrm{m}$ disk-shaped dot. **c** Addition energy versus electron number for two different dots with $D = 0.50$ and $0.44\,\mu\mathrm{m}$. Adapted from [1391]

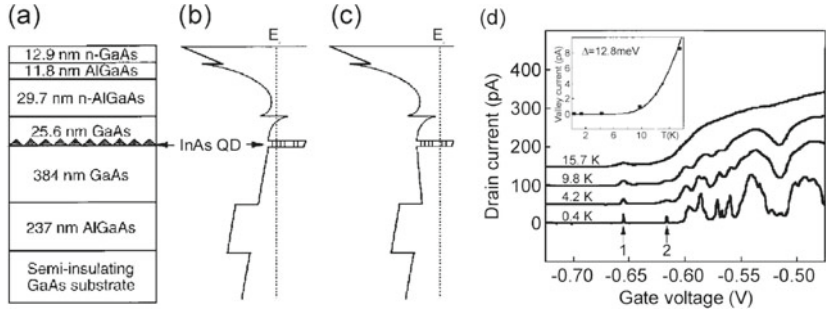

Fig. 14.31 **a** Schematic layer sequence of epitaxial structure comprising a n-AlGaAs/GaAs heterointerface with a two-dimensional electron gas and a layer of InAs/GaAs quantum dots. **b** and **c** are corresponding band diagrams with no gate bias and gate voltage below the critical value, respectively. **d** Experimental dependence of drain current on gate voltage in a split-gate structure at a drain source voltage of $10\,\mu\mathrm{V}$. *Inset*: Dependence of valley current on temperature (*squares*) with theoretical fit. Reprinted with permission from [1392], ©1997 AIP

$$E_{21} = \langle 00|W_{ee}|00\rangle = \iint \Psi_0^2(\mathbf{r}_e^1)\, W_{ee}(\mathbf{r}_e^1, \mathbf{r}_e^2)\, \Psi_0^2(\mathbf{r}_e^2)\, \mathrm{d}^3\mathbf{r}_e^1\, \mathrm{d}^3\mathbf{r}_e^2\,, \tag{14.23}$$

where W_{ee} denotes the Coulomb interaction of the two electrons and Ψ_0 the ground state (single particle) electron wavefunction. The matrix element gives an upper bound for the charging energy since the wavefunctions will rearrange to lower their overlap and the repulsive Coulomb interaction. For lens-shaped InAs/GaAs quantum dots with radius 25 nm a charging energy of about 30 meV has been predicted.

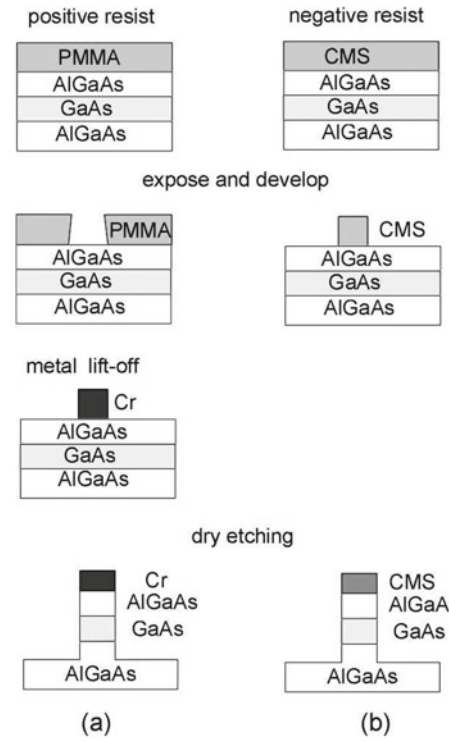

Fig. 14.32 Lithography and etching techniques for the fabrication of semiconductor structures

14.4.3 Self-Assembled Preparation

The preparation methods for QDs split into top-down (lithography and etching) and bottom-up (self-assembly) methods. The latter achieve typically smaller sizes and require less effort (at least concerning the machinery).

Artificial Patterning

Using artificial patterning, based on lithography and etching (Fig. 14.32), quantum dots of arbitrary shape can be made (Fig. 14.33). Due to defects introduced by high-energy ions during reactive ion etching the quantum efficiency of such structures is very low when they are very small. Using wet-chemical etching techniques the damage can be significantly lowered but not completely avoided. Since the QDs have to compete with other structures that can be made structurally perfect, this is not acceptable.

Template Growth

Template growth is another technique for the formation of nanostructures. Here, a mesoscopic structure is fabricated by conventional means. The nanostructure is created using size-reduction mechanisms, e.g., faceting, (Fig. 14.34). This method can potentially suffer from low template density, irregularities of the template, and problems of reproducibility.

Colloids

Another successful route to nanocrystals is the doping of glasses with subsequent annealing (color filters). When nanocrystals are prepared in a sol-gel process, the nanoparticles are present as a colloid in wet solution. With the help of suitable stabilizing agents they are prevented from sticking to each other

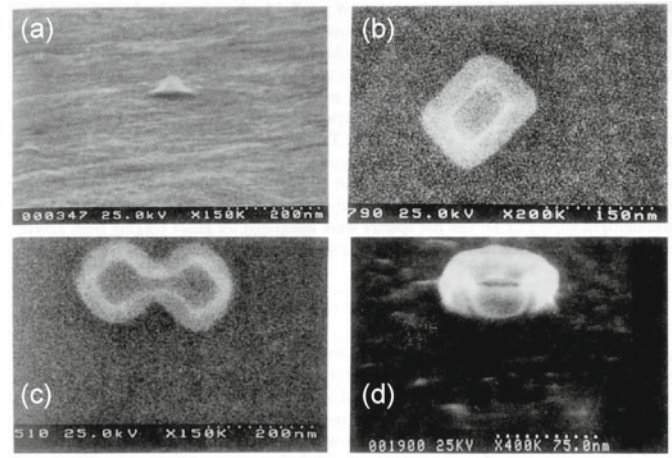

Fig. 14.33 Quantum dots of various shapes created by lithography and etching techniques. From [1393]

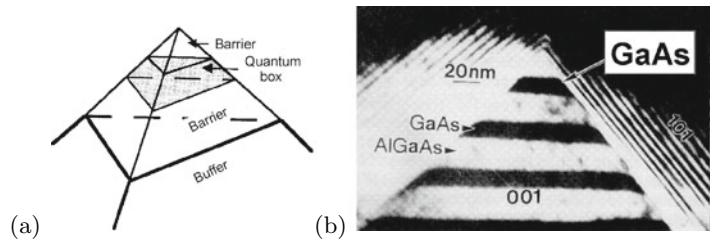

Fig. 14.34 **a** Schematic representation of growth on top of a predefined template, **b** cross-sectional TEM of quantum dot formation at the apex. Reprinted with permission from [1394], ©1992 MRS

and can be handled in ensembles and also individually. Such nanocrystals have been synthesized and investigated in particular for II–VI (Fig. 14.35a) and halide perovskite (Fig. 14.35b) semiconductors.

Mismatched Epitaxy

The self-assembly (or self-organization) relies on strained heterostructures that achieve energy minimization by island growth on a wetting layer (Stranski-Krastanow growth mode, see Sect. 12.2.3 and [1339]). Additional ordering mechanisms [1397, 1398] lead to ensembles that are homogeneous in size[2] [1399] and shape [1400] (Fig. 14.36).

When a thin layer of a semiconductor is grown on top of a flat substrate with different lattice constant, the layer suffers a tetragonal distortion (Sect. 5.3.3). Strain can only relax along the growth direction (Fig. 14.37). If the strain energy is too large (highly strained layer or large thickness), plastic relaxation via dislocation formation occurs. If there is island geometry, strain can relax in all three directions and about 50% more strain energy can relax, thus making this type of relaxation energetically favorable. When the island is embedded in the host matrix, the strain energy is similar to the 2D case and the matrix becomes strained (metastable state).

When such QD layers are vertically stacked, the individual quantum dots grow on top of each other (Fig. 14.38) if the separation is not too large (Fig. 14.40). This effect is due to the effect of the underlying QD. In the case of InAs/GaAs (compressive strain), the buried QD stretches the surface above it (tensile surface strain). Thus, atoms impinging in the next QD layer find a smaller strain right on top of the buried QDs. In STM images of the cross section through (XSTM) such a stack (Fig. 14.39) individual indium atoms are visible and the shape can be analyzed in detail [1402].

[2]The ordering in size is remarkable. Typically Ostwald ripening (due to the Gibbs-Thomson effect; smaller droplets have larger vapor pressure and dissolve, larger droplets accordingly grow) occurs in an ensemble of droplets or nuclei. In the case of strained QDs, surface energy terms stabilize a certain QD size.

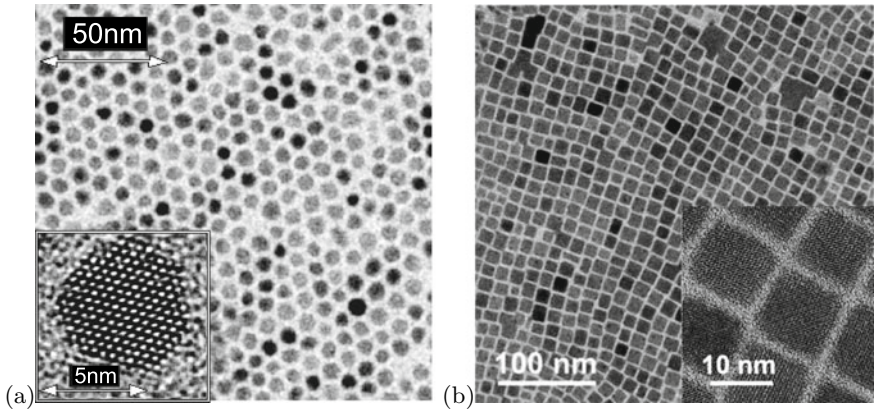

Fig. 14.35 **a** CdSe colloidal (hexagonal) nanoparticles. From [1395]. **b** $CsPbBr_3$ perovskite (cubic) colloidal nanocrystals. Adapted from [1396] under Creative Commons Attribution (CC BY 4.0) license

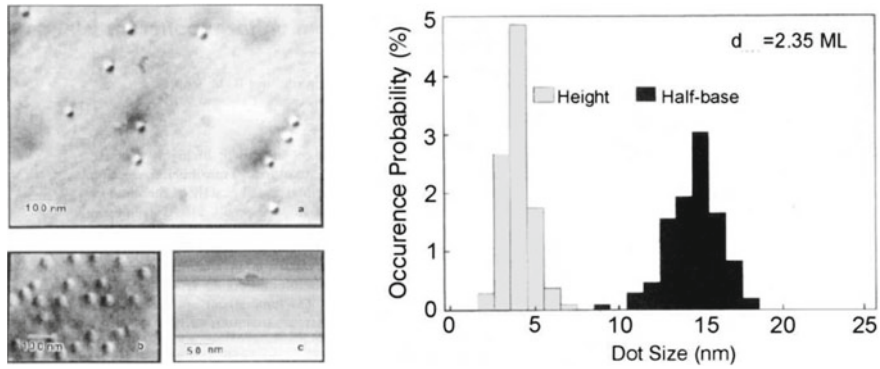

Fig. 14.36 Self-organized formation of InGaAs/GaAs quantum dots during epitaxy. *Left*: Plan-view and cross-sectional transmission electron micrographs. *Right*: Histogram of vertical and lateral size of the quantum dots. Reprinted with permission from [1401], ©1993 AIP

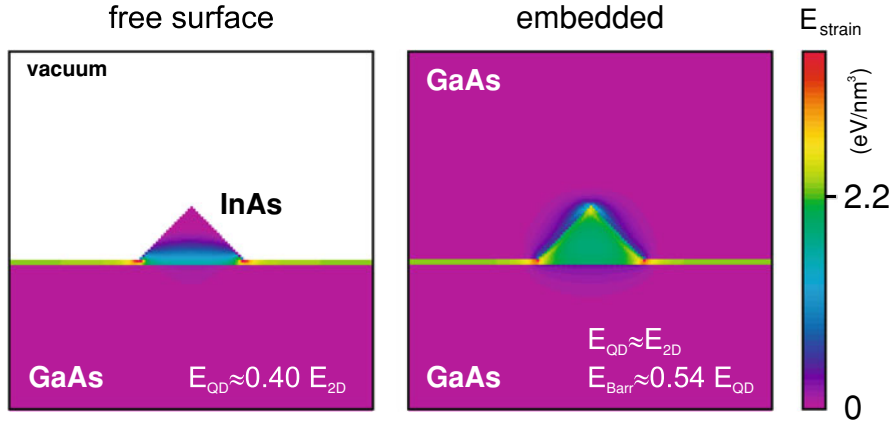

Fig. 14.37 Distribution of strain energy for (*left*) uncapped island and (*right*) island embedded in host matrix. Numerical values are for InAs/GaAs

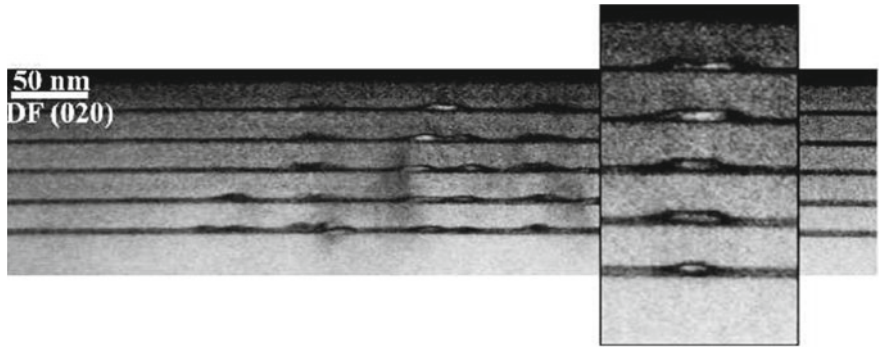

Fig. 14.38 Cross-sectional TEM image of a stack of five layers of quantum dots. Due to strain effects, vertical arrangement is achieved

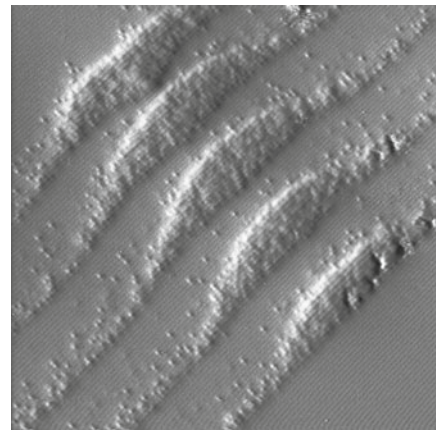

Fig. 14.39 Cross-sectional STM image of a stack of five InAs quantum dots in a GaAs matrix. Individual In atoms can be observed in-between the wetting layers and the quantum dots. Each quantum dot layer was formed by growing 2.4 ML of InAs. The intended distance between the quantum dot layers was 10 nm. Image size is $55 \times 55\,\mathrm{nm}^2$. Reprinted with permission from [1402], ©2003 AIP

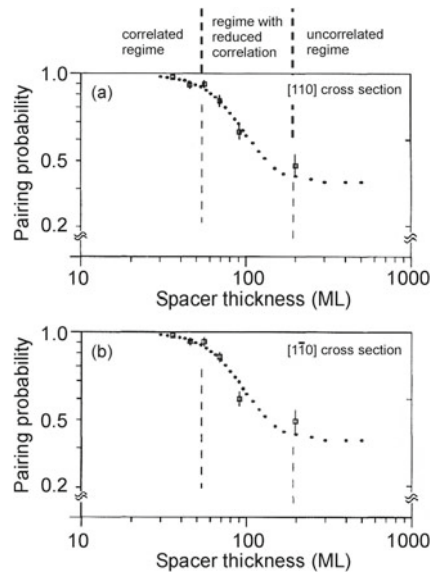

Fig. 14.40 Experimentally observed pairing probability in MBE-grown stacks of InAs/GaAs quantum dots as a function of the spacer-layer thickness. Data are taken from (**a**) (110) and (**b**) (1–10) cross-sectional TEM images. The *filled circles* are fit to data from theory of correlated island formation under strain fields. Reprinted with permission from [1403], ©1995 APS

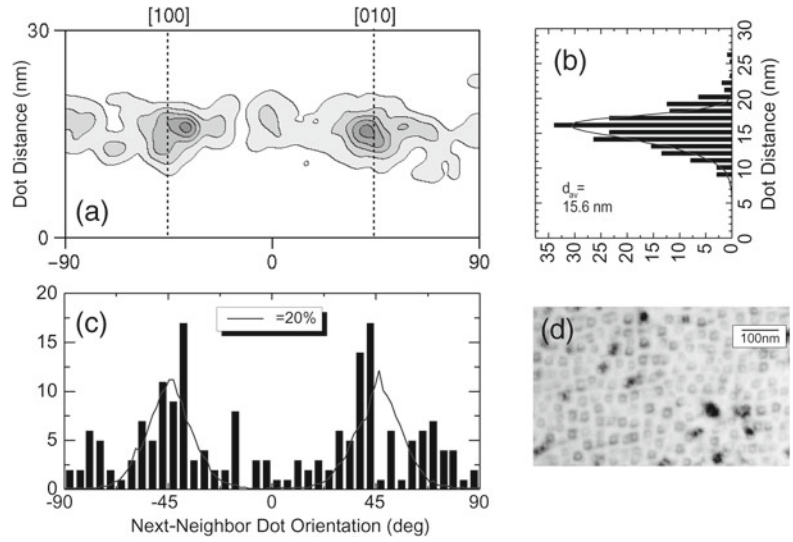

Fig. 14.41 Lateral ordering of QD array. **d** Plan-view TEM of QD array on which the statistical evaluation is based. **a** Two-dimensional histogram of QDs as a function of the nearest-neighbor distance and direction, (**b**, **c**) projections of part (**a**). *Solid lines* in (**b**) and (**c**) are theory for square array with $\sigma = 20\%$ deviation from ideal position. Adapted from [1339, 1397]

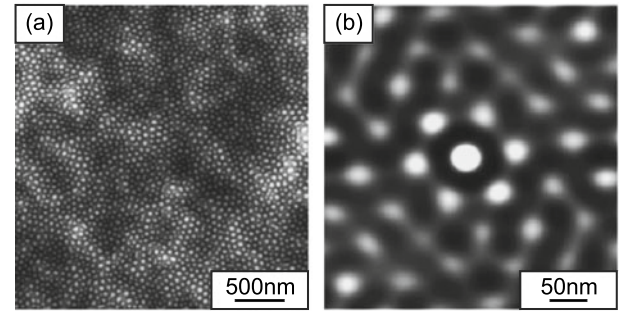

Fig. 14.42 **a** AFM image of a Si (001) substrate after 960 min of ion sputtering (1.2 keV Ar^+, normal incidence). **b** Two-dimensional autocorrelation function from a $400 \times 400\,nm^2$ area of image in part (**a**). Adapted from [1406] with permission, ©2001 AIP

The vertical arrangement can lead to further ordering since a homogenization in lateral position takes place. If two QDs in the first layers are very close, their strain fields overlap and the second layer 'sees' only one QD.

The lateral (in-plane) ordering of the QDs with respect to each other occurs in square or hexagonal patterns and is mediated via strain interaction through the substrate. The interaction energy is fairly small, leading only to short-range in-plane order [1397] as shown in Fig. 14.41. The in-plane ordering can be improved up to the point that regular one- or two-dimensional arrays form or individual quantum dots are placed on designated positions using directed self-assembly [1339]. Among others, dislocation networks buried under the growth surface of the nanostructure, surface patterning and modification have been used to direct the QD positioning.

Ion-Beam Erosion

During the erosion of a surface with low-energy ion beam sputtering ordered patterns of dots appear [1404–1407]. Isotropic [1408] and hexagonal [1404, 1406] (Fig. 14.42) near-range ordering has been observed. The pattern formation mechanism is based on the morphology-dependent sputter yield and further mechanisms of mass redistribution [1409]. Also linear patterns have been reported [1410].

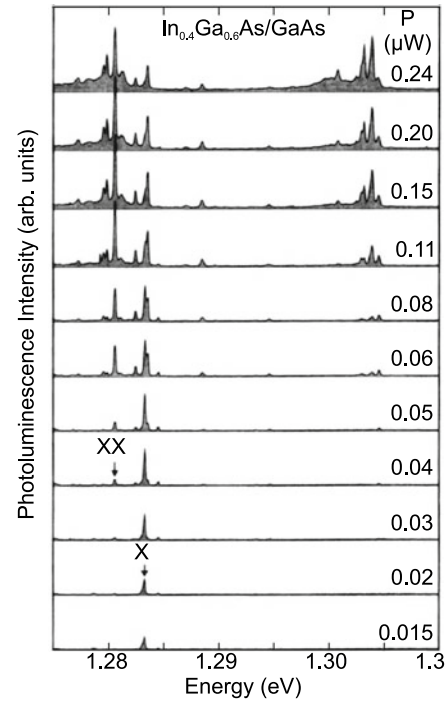

Fig. 14.43 Optical emission spectra ($T = 2.3\,\mathrm{K}$) of a single InGaAs/GaAs quantum dot at different laser excitation levels P as labeled. The single exciton (X) and biexciton (XX) lines are indicated. Adapted from [1411]

14.4.4 Optical Properties

The optical properties of QDs are related to their electronic density of states. In particular, optical transitions are allowed only at discrete energies due to the zero-dimensional density of states.

Photoluminescence from a single QD is shown in Fig. 14.43. The δ-like sharp transition is strictly true only in the limit of small carrier numbers ($\ll 1$ exciton per dot on average) since otherwise many-body effects come into play that can encompass recombination from charged excitons or multiexcitons. At very low excitation density the recombination spectrum consists only of the one-exciton (X) line. With increasing excitation density small satellites on either side of the X-line develop that are attributed to charged excitons (trions) X^+ and X^-. On the low-energy side, the biexciton (XX) appears. Eventually, the excited states are populated and a multitude of states contribute with rich fine structure. In bulk material the biexciton (Sect. 9.7.10) is typically a bound state, i.e. its recombination energy E_{XX} is lower than that of the exciton E_X. A similar situation is present in Fig. 14.43. It was pointed out in [1412] that in QDs the biexciton recombination energy can also be *larger* than the exciton recombination energy. In [1413] the modification of the QD confinement potential of InAs/GaAs QDs by annealing was reported. The exciton binding energy (E_X-E_{XX}) is tuned from positive ('normal') to negative values upon annealing (Fig. 14.44).

The charging state of the exciton can be controlled in a field-effect structure. The recombination energy is modified due to Coulomb and exchange effects with the additional carriers. In charge-tunable quantum dots [1414] and rings [1415] exciton emission has been observed in dependence of the number of additional electrons. The electron population can be controlled in a Schottky-diode-like structure through the manipulation of the Fermi level with the bias voltage. At high negative bias all charge carriers tunnel out of the ring and no exciton emission is observed. A variation of the bias then leads to an average population with $N = 1, 2, 3, \ldots$ electrons. The recombination of additional laser-excited

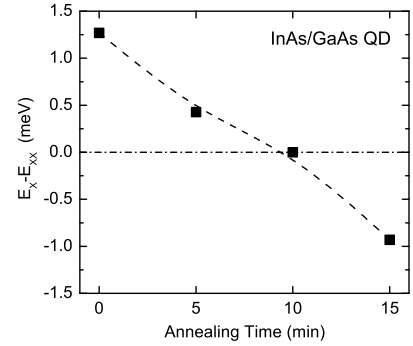

Fig. 14.44 Biexciton binding energy determined for a single InAs/GaAs quantum dot for various annealing times. Data from [1413]

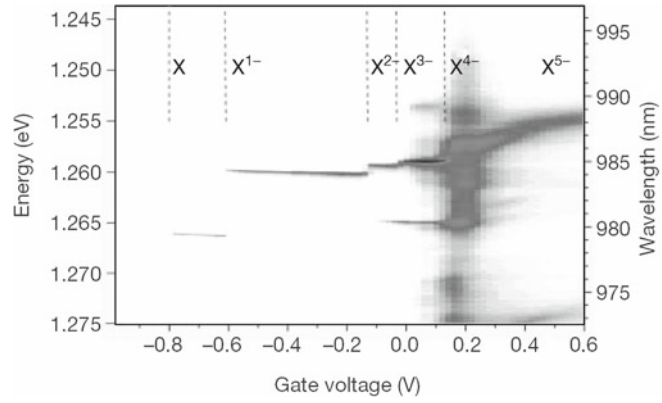

Fig. 14.45 Luminescence of charged excitons from a single quantum ring at $T = 4.2\,\mathrm{K}$ versus the bias voltage with which the number of electrons in the quantum dot N is tuned from zero to $N > 3$. Adapted from [1415], reprinted with permission, ©2000, Springer Nature

excitons depends (due to the Coulomb interaction) on the number of the electrons present (Fig. 14.45). The singly negatively charged exciton X^- is also called a trion.

The interaction of a spin with an exciton in a CdTe quantum dot has been observed in [1416]. If the CdTe quantum dot is pure, a single line arises. If the dot contains a single Mn atom, the exchange interaction of the exciton with the Mn $S = 5/2$ spin leads to a six-fold splitting of the exciton line (Fig. 14.46. In an external magnetic field a splitting into a total of twelve lines due to Zeeman effect at the Mn spin is observed.

In a QD ensemble, optical transitions are inhomogeneously broadened due to fluctuations in the QD size and the size dependence of the confinement energies (Fig. 14.47). Interband transitions involving electrons and holes suffer from the variation of the electron and hole energies:

$$\sigma_E \propto \left(\left| \frac{\partial E_\mathrm{e}}{\partial L} \right| + \left| \frac{\partial E_\mathrm{h}}{\partial L} \right| \right) \delta L \ . \tag{14.24}$$

A typical relative size inhomogeneity of σ_L/L of 7% leads to several tens of meV broadening. Additional to broadening due to different sizes fluctuations of the quantum dot shape can also play a role. The confinement effect leads to an increase of the recombination energy with decreasing quantum-dot size. This effect is nicely demonstrated with colloidal quantum dots of different size as shown in Fig. 14.48.

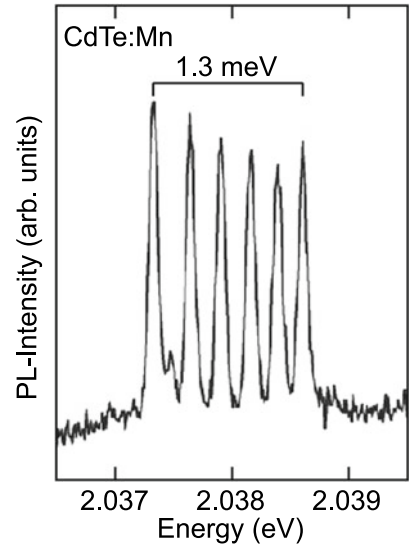

Fig. 14.46 Photoluminescence spectrum of a single CdTe/ZnSe quantum dot containing a single Mn atom ($T = 5\,\mathrm{K}$). Adapted from [1416], reprinted with permission, ©2004 APS

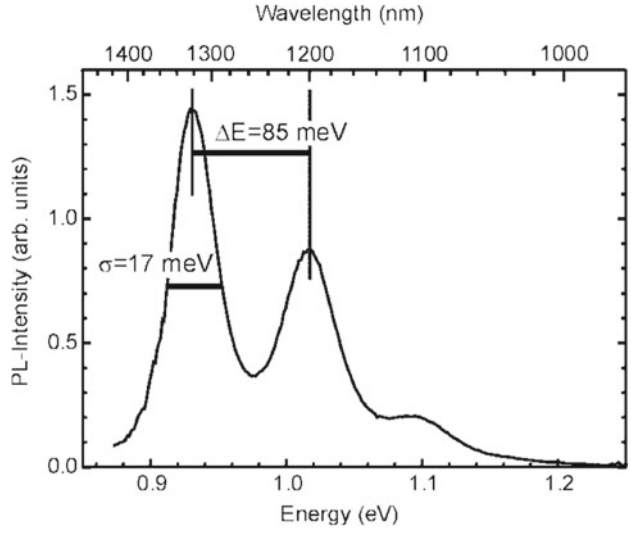

Fig. 14.47 Ensemble photoluminescence spectrum ($T = 293\,\mathrm{K}$, excitation density $500\,\mathrm{W/cm^2}$) of InAs/GaAs QDs

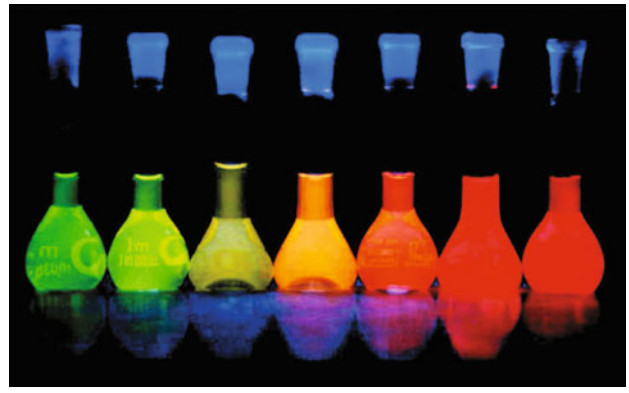

Fig. 14.48 Luminescence (under UV excitation) from flasks of colloidal CdTe quantum dots with increasing size (from left to right). From [1395]